npj Computational Materials

www.nature.com/npjcompumats

ARTICLE OPEN

Check for updates

Environmental screening and ligand-field effects to magnetism in CrI_3 monolayer

D. Soriano[1,2], A. N. Rudenko[1,3], M. I. Katsnelson[1,3] and M. Rösner[1]✉

We study the microscopic origin of magnetism in suspended and dielectrically embedded CrI_3 monolayer by down-folding minimal generalized Hubbard models from ab initio calculations using the constrained random phase approximation. These models are capable of describing the formation of localized magnetic moments in CrI_3 and of reproducing electronic properties of direct ab initio calculations. Utilizing the magnet force theorem, we find a multi-orbital super-exchange mechanism as the origin of magnetism in CrI_3 resulting from an interplay between ferro- and anti-ferromagnetic Cr-Cr *d* coupling channels, which is decisively affected by the ligand *p* orbitals. We show how environmental screening, such as resulting from encapsulation with hexagonal boron nitride, affects the Coulomb interaction in the film and how this controls its magnetic properties. Driven by a non-monotonic interplay between nearest and next-nearest neighbor exchange interactions we find the magnon dispersion and the Curie temperature to be non-trivially affected by the environmental screening.

npj Computational Materials (2021)7:162 ; https://doi.org/10.1038/s41524-021-00631-4

INTRODUCTION

Ferromagnetic (FM) layered materials hold high promises for becoming one of the key ingredients in future spintronic nanodevices[1–4] based on van-der-Waals heterostructures. Recent observations of magnons in thin layers of chromium trihalides via inelastic electron tunneling spectroscopy (IETS)[1,5] and magneto-Raman spectroscopy[6] have also opened new ways to explore magnon-based low-consumption spintronics at the two-dimensional (2D) limit[7]. Whether or how the magnetic properties are modified or stabilized in these heterostructures is, however, still under debate. Recently reported theoretical predictions to suggest, for instance, a strong dependence of the magneto-optical response on the film thickness and the spin–orbit coupling of CrI_3[8], while recent experimental studies point towards the possibility to tune the magnetic properties of monolayer and bilayer CrI_3 using electrostatic gating[9–12]. These observations highlight the importance of addressing how the environment of layered magnetic systems modifies their electronic and magnetic properties via proximity, gating, or screening effects.

For the case of chromium trihalides, CrX_3 (X = I, Br, Cl), the nearest neighbor magnetic exchange couplings have been theoretically reported to be between 1 and 3.2 meV[13–18] depending on the material and calculation scheme, which renders rigorous theoretical descriptions absolutely necessary. This holds especially with respect to the Coulomb interactions in a layered material, which are enhanced due to reduced polarization in the surrounding. At the same time changes to the environmental polarization and thus to the environmental screening can significantly modify the Coulomb interaction within the layered material. Thus, properties of layered materials affected by the Coulomb interaction, such as the formation of excitons and plasmons or the stabilization of charge and superconducting order, are in principle strongly dependent on the material's environment allowing for Coulomb engineering of these many-body properties[19–24]. So far it is not known how efficient Coulomb engineering can be for tailoring the magnetic ground state or magnonic excitations of layered magnetic systems. For the case of CrI_3, both can be described by effective spin Hamiltonians describing exchange interactions between the Cr atoms as the spin carriers. Thus any changes from environmental screening to the exchange couplings of this effective Hamiltonian can give rise to changes in the magnetic transition temperature or the magnon spectrum opening new routes towards the control and potential tailoring of magnetic properties of chromium trihalides.

Computationally it is, however, a non-trivial task to reliably study how screening from the environment modifies the exchange couplings, as this is beyond the capabilities of conventional density functional theory (DFT) based approaches, which describe environmentally induced modifications to the Coulomb interactions and thus to the magnetic properties only poorly. To overcome these DFT-based shortcomings, higher-level theories, such as the *GW* approximation, are needed which take screening explicitly on the level of the random phase approximation (RPA) into account. Full ab initio *GW* calculations for layered heterostructures are, however, not feasible due to the large supercells needed to account for lattice mismatches between the involved materials. We utilize a multi-step approach to overcome these computational problems of the conventional approaches to study the impact of Coulomb interactions on the magnetic properties of suspended and dielectrically embedded monolayer CrI_3. We start from spin-unpolarized ab initio band structure calculations for monolayer CrI_3 using DFT, which we use to down-fold two minimal models defined by localized Wannier orbitals describing the Cr *d* states only and a combined $(d+p)$-basis also taking the I *p* states into account. After constructing the corresponding Coulomb tensors from constrained RPA (cRPA) calculations we solve the resulting multi-orbital Hubbard models within mean-field Hartree–Fock (HF) theory. The resulting interacting and spin-resolved quasi-particle band structures are used afterward to evaluate the orbitally resolved magnetic exchange

[1]Radboud University, Institute for Molecules and Materials, Heyendaalseweg 135, 6525 AJ Nijmegen, The Netherlands. [2]Università di Pisa, Dipartimento di Ingegneria dell'Informazione, Via Caruso, 56122 Pisa, Italy. [3]Department of Theoretical Physics and Applied Mathematics, Ural Federal University, 620002 Ekaterinburg, Russia. ✉email: m.roesner@science.ru.nl

Published in partnership with the Shanghai Institute of Ceramics of the Chinese Academy of Sciences

interactions using the magnetic force theorem (MFT). Using our Wannier function continuum electrostatics (WFCE) approach we additionally include the environmental screening effects to the Coulomb interactions, which finally allows us to study how the microscopic exchange coupling channels, the magnetic transition temperature, and the magnon dispersions are affected by different parts of the Coulomb tensor and/or by the dielectric encapsulation of the CrI_3 monolayer. This combination of carefully validated state-of-the-art approaches allows us to microscopically study magnetism in CrI_3 heterostructures.

RESULTS

Ab initio calculations

In the crystal structure of monolayer CrI_3, the Cr atoms are arranged on a honeycomb lattice surrounded by the I ligands forming an edge-sharing octahedral environment around each metal ion, as depicted in Fig. 1a. The ligand field splits the Cr *d*-orbitals into two sets, namely, the t_{2g} (d_{xy}, d_{xz}, d_{yz}) and the e_g ($d_{x^2-y^2}$, d_{z^2})[13]. Spin un-polarized first-principles calculations in the generalized gradient approximation (GGA) level predict a metallic ground state with half-filled bands of predominantly Cr t_{2g} character separated by sizable gaps from fully occupied bands of mostly I *p* character and unoccupied bands of Cr e_g type, as shown in the atomic resolved density of states (DOS) in Fig. 1b. Spin-polarized calculations in the GGAs + *U* approximation[25] shift down the majority spin t_{2g} bands which hybridize with the ligand *p*-bands. The unoccupied majority spin e_g bands appear at approximately 1.5 eV above the valence states followed by the minority spin t_{2g} and e_g bands, respectively, resulting in an FM insulating state, as depicted in Fig. 1 (c). Although LSDA+*U* approaches seem to reasonably describe the magnetic properties of CrI_3, its validity still needs to be benchmarked with higher-level

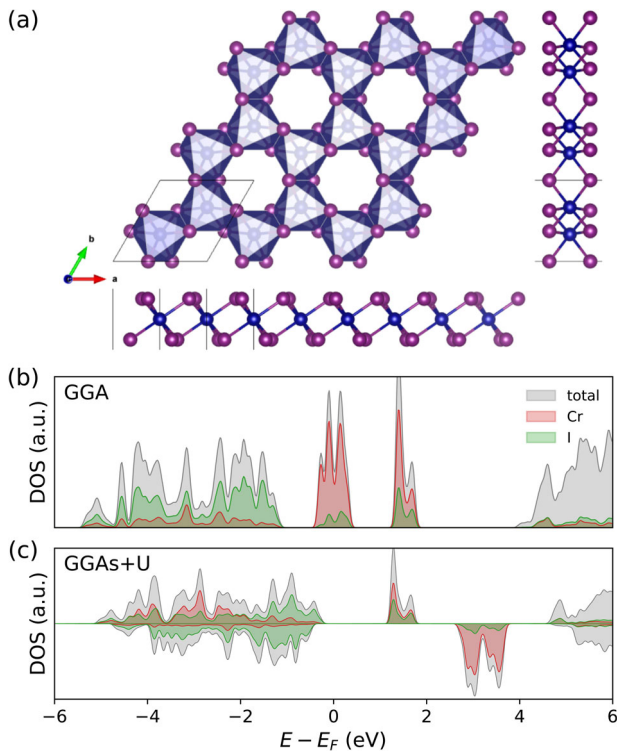

Fig. 1 CrI_3 lattice and ab initio electronic structure. a Lattice structure with primitive unit cell visualized using VESTA[56]. **b** GGA density of states with I and Cr contributions. **c** GGAs + *U* density of states separated into spin up and down using $U = 4$ eV and $J = 0.6$ eV.

theories such as dynamical mean-field theory, as the local Coulomb repulsion, *U* is rather large compared to the t_{2g} bandwidth as discussed in detail later. Thus, to fully microscopically understand each part of the problem, ranging from hybridization effects to the Coulomb tensor to the choice of basis set, we proceed in the following with a down-folding procedure to generate reliable material-realistic minimal models.

Model Hamiltonian

In the following, we will construct model Hamiltonians of the form

$$\mathcal{H} = \mathcal{H}^W + \mathcal{H}^U - \mathcal{H}^{DC}. \tag{1}$$

with $\mathcal{H}^W$ describing the non-interacting kinetic terms and $\mathcal{H}^U$ describing the local Coulomb interactions of the Cr *d* orbitals. Depending on the chosen basis we additionally use a double-counting correction $\mathcal{H}^{DC}$. The non-interacting part of the Hamiltonian is defined by long-range hopping matrix elements t_{mn} and reads

$$\mathcal{H}^W = \sum_{\mathbf{k},m,n,\sigma} t_{mn}(k) d^\dagger_{m\sigma}(\mathbf{k}) d_{n\sigma}(\mathbf{k}), \tag{2}$$

while the Coulomb term takes local density-density $U_{mm'}$ and Hund's exchange $J^{\mathrm{H}}_{mm'}$ interactions on the Cr atoms into account and is defined by

$$\begin{aligned}\mathcal{H}^U = & \tfrac{1}{2}\sum_{m,\sigma} U_{mm}\hat{n}_{m\sigma}\hat{n}_{m\bar{\sigma}} \\ & + \tfrac{1}{2}\sum_{m\neq m',\sigma} U_{mm'}\hat{n}_{m\sigma}\hat{n}_{m'\bar{\sigma}} \\ & + \tfrac{1}{2}\sum_{m\neq m',\sigma} (U_{mm'} - J^{\mathrm{H}}_{mm'})\hat{n}_{m\sigma}\hat{n}_{m'\sigma} \\ & - \tfrac{1}{2}\sum_{m\neq m',\sigma} (J^{\mathrm{H}}_{mm'}) d^\dagger_{m\sigma} d_{m\bar{\sigma}} d^\dagger_{m'\bar{\sigma}} d_{m'\sigma},\end{aligned} \tag{3}$$

where $\hat{n}_\sigma = d^\dagger_{m\sigma} d_{m\sigma}$ is the number operator and σ is the spin index. These Hamiltonians are solved within a mean-field HF ansatz and analyzed in terms of its microscopic magnetic properties as described in the "Methods" section.

Basis sets and non-interacting Hamiltonians

Motivated by the non-magnetic ab initio DOS depicted in Fig. 1b, we utilize two minimal basis sets: one including only effective Cr *d* Wannier orbitals and a second one also including I *p* states, which are, respectively, referred to as *d*-only and (*d* + *p*) models in the following. To this end, we start with conventional DFT calculations utilizing the Perdew–Burke–Ernzerhof GGA exchange-correlation functional[26] within a PAW basis[27,28] as implemented in the Vienna Ab initio Simulation Package (VASP)[29,30] for CrI_3 monolayers with a lattice constant of $a_0 \approx 6.97$ Å embedded in a supercell with a height of 35 Å. We use $(16 \times 16 \times 1)$ *k*-meshes together with an energy cutoff of 230 eV and apply a Methfessel–Paxton smearing of $\sigma = 0.02$ eV. For the *d*-only model, we project the 10 Kohn–Sham states per spin between −0.8 eV and +2.2 eV (inner and outer Wannierization windows) onto 10 Cr-localized *d* orbitals (with a rotating axis parallel to the tetragonal main axis) and maximally localize them afterward using the WANNIER90 package[31]. For the (*d* + *p*)-model, we similarly project all Kohn–Sham states between −6.0 and +2.2 eV to Cr-centered *d* orbitals as well as to I-centered *p* orbitals. In this case, we do not perform a total maximal localization of the total spread of all Wannier orbitals since it would increase the localization of the I *p* orbitals at the cost of delocalization of Cr *d* orbitals. This way we get in both models maximally localized Cr *d* orbitals (at the cost of delocalized *p* orbitals in the (*d* + *p*)-model). These Wannier orbitals are used in a subsequent step to calculate the needed hopping matrix elements for the definition of $\mathcal{H}^W$. As shown in Supplementary Methods 1, the resulting Wannier models perfectly interpolate all

Table 1. Bare (v/J^H) and cRPA screened (U/J^H) local Coulomb interaction matrix elements from the *d*-only basis set in eV.

J^H/v	t_{2g}	t_{2g}	t_{2g}	e_g	e_g
t_{2g}	15.501	14.384	14.383	13.086	12.783
t_{2g}	*0.535*	15.506	14.386	13.086	12.786
t_{2g}	*0.535*	*0.535*	15.505	12.635	13.236
e_g	*0.318*	*0.318*	*0.515*	12.313	11.288
e_g	*0.449*	*0.449*	*0.252*	*0.512*	12.312
J^H/U	t_{2g}	t_{2g}	t_{2g}	e_g	e_g
t_{2g}	3.546	2.531	2.531	2.669	2.419
t_{2g}	*0.487*	3.547	2.532	2.668	2.421
t_{2g}	*0.487*	*0.487*	3.547	2.296	2.793
e_g	*0.301*	*0.301*	*0.465*	3.108	2.224
e_g	*0.410*	*0.410*	*0.247*	*0.442*	3.108

Density-density matrix elements are listed on the upper triangle and Hund's exchange elements are underlined and italic.

Kohn–Sham states between −0.8 eV and +2.2 eV in the *d*-only model as well as all Kohn–Sham states between −6.0 eV and +2.2 eV in the (*d* + *p*)-model.

Constrained random phase approximation

The Coulomb interaction matrix elements of $\mathcal{H}^U$ are evaluated using the Cr *d* Wannier orbitals from these two models within the cRPA scheme[32] according to

$$U_{ijkl} = \langle w_i w_j | \mathcal{U} | w_k w_l \rangle. \tag{4}$$

Here, $\mathcal{U}$ represents the partially screened Coulomb interaction defined by

$$\mathcal{U} = \mathcal{V} + \mathcal{V}\,\Pi_{\text{rest}}\,\mathcal{U}, \tag{5}$$

with $\mathcal{V}$ being the bare Coulomb interaction and Π_{rest} the partial or rest-polarization from all states except those of the correlated subspace defined by the Cr *d* states. Π_{rest} thus describes screening from all other Cr as well as all I states including a significant amount of empty states from the full Kohn–Sham basis. In detail, we use in total 128 bands and define Π_{rest} by explicitly excluding all Kohn–Sham states between −0.5 and 3 eV from the full polarization. To this end, we use a recent cRPA implementation by Kaltak available in VASP[33] (see Supplementary Methods 2 for further details). This way we remove the unrealistically strong metallic screening of the half-occupied t_{2g} band of the spin-unpolarized GGA starting point. From this we can extract the full rank-4 Coulomb tensor in the basis of the correlated Cr *d* states. Within $\mathcal{H}^U$ we restrict ourselves however to static local density-density elements $U_{mm'} = U_{mm'm'm}$ and local Hund's exchange elements $J^H_{mm'} = U_{mm'mm'}$ with *m* and *m*′ labeling *d* orbitals on the same Cr atom. As shown in ref. [34], non-local interactions do not significantly modify the magnon dispersions of bulk CrI_3, while the local interactions have a strong impact on the latter. We thus neglect both non-local density–density and non-local Hund's interactions here and use only the corresponding onsite interactions. Casula et al.[35] furthermore showed that using $\mathcal{U}(\omega = 0)$ instead of the fully retarded $\mathcal{U}(\omega)$ is justified when renormalized hopping parameters are utilized. The corresponding renormalization factor was shown to scale with the characteristic cRPA plasmon frequency ω_p. In the Supplementary Methods 3, we show that for CrI_3 ω_p is rather large, which renders these renormalizations small here. We therefore neglect them in the following.

Minimal Cr *d*-only basis

We start with analyzing the local bare and cRPA screened density-density Coulomb matrix elements as obtained from the *d*-only basis. The full matrices are shown in Table 1 together with the corresponding Hund's exchange elements. In all cases the resulting density–density matrices are approximately of the form

$$v_{mm'} \approx \begin{pmatrix} v_t & v_t - 2j^H_t & v_t - 2j^H_t & v_{et} - 2j^H_1 & v_{et} - 2j^H_2 \\ v_t - 2j^H_t & v_t & v_t - 2j^H_t & v_{et} - 2j^H_1 & v_{et} - 2j^H_2 \\ v_t - 2j^H_t & v_t - 2j^H_t & v_t & v_{et} - 2j^H_3 & v_{et} - 2j^H_4 \\ v_{et} - 2j^H_1 & v_{et} - 2j^H_1 & v_{et} - 2j^H_3 & v_e & v_e - 2j^H_e \\ v_{et} - 2j^H_2 & v_{et} - 2j^H_2 & v_{et} - 2j^H_4 & v_e - 2j^H_e & v_e \end{pmatrix}, \tag{6}$$

where v_t (j^H_t) and v_e (j^H_e) are intra-orbital density–density (inter-orbital Hund's exchange) matrix elements within the t_{2g} and e_g manifolds, respectively, $v_{et} = 1/2(v_e + v_t)$, and $j^H_{1\ldots4}$ are inter-orbital Hund's exchange elements between the two manifolds. This form of the density–density Coulomb matrix is similar to the one obtained for a fully rotational-invariant *d* shell which is here, however, perturbed due to the ligand-induced crystal-filed splitting. Therefore, instead of five U_0, $J^H_{1\ldots4}$ or three U_0, F_2, F_4[36] parameters we need here eight to represent the full density–density matrix. As a result, the t_{2g} and e_g channels themselves are easily parameterized using two Hubbard–Kanamori parameters (*v* and J^H). The inter-channel elements show, however, a significant orbital dependence which can be represented by the four $j^H_{1\ldots4}$ Hund's exchange elements.

Since the Wannier orbital spread $\Omega_a = \langle w_a|r^2|w_a\rangle - \langle w_a|r|w_a\rangle^2$[31] of the t_{2g} wave functions ($\Omega_{t_{2g}} \approx 3$ Å^2) is smaller then the corresponding e_g one ($\Omega_{eg} \approx 5.3$ Å^2) the bare intra-orbital density–density elements $v_t \approx 15.5$ eV are larger than the $v_e \approx$ 12.3 eV elements and also represent the largest elements in $v_{mm'}$. This is also reflected in the intra-channel $j^H_t \approx 0.54$ eV and $j^H_e \approx 0.51$ eV elements which are, however, still rather similar. The inter-channel $j^H_{1\ldots4}$ vary between about 0.25 and 0.47 eV. We note that these bare Hund's exchange interactions are significantly smaller than the approximated values in bulk Cr of $J^H \approx 0.75$ eV[37], which we attribute here to the enhanced Wannier function spread of the effective Cr *d*-only basis.

The cRPA density-density matrix elements $U_{mm'}$ are significantly reduced by factors between 1/4 to nearly 1/6 by the rest-space screening from the other Cr and I states. Although this effective screening is strongly orbital dependent, it does not change the overall orbital structure of the Coulomb matrix depicted in Eq. (6). We find $U_t \approx 3.6$ eV and $U_e \approx 3.1$ eV, which are still rather large compared to the bandwidth of the half-filled Cr t_{2g} band of about 1 eV. Thus even taking cRPA screening into account correlation effects can be expected to play an important role. The screened Hund's exchange interactions, $J^H_t \approx 0.49$ eV and $J^H_e \approx 0.44$ eV, are reduced by no more than 10% in comparison to the bare values, which also holds for the inter-channel ones. The nearest-neighbor cRPA screened density–density interactions are nearly orbital independent $U_{01} \approx 1.4$ eV. The nearest-neighbor Hund's interactions are vanishingly small ranging between $J_{01} \approx 1$ and 7 meV.

We proceed with analyzing how the local cRPA-screened Coulomb interactions affect the band structure of the Cr *d*-only model within the mean-field theory. As depicted in Fig. 2 the Coulomb interactions drive the systems into an insulator with a sizeable bandgap and the same band ordering as known from LSDA(+*U*) calculations (i.e., fully occupied t_{2g} followed by completely empty $e_{g,\uparrow}$, $t_{2g,\downarrow}$, and $e_{g,\downarrow}$ manifolds). On a qualitative level, this minimal basis thus seems to be capable of reproducing the Cr *d* band structure of full ab initio calculations. To analyze to what extent this minimal model is also capable of reproducing the super-exchange mechanism responsible for the FM ordering in

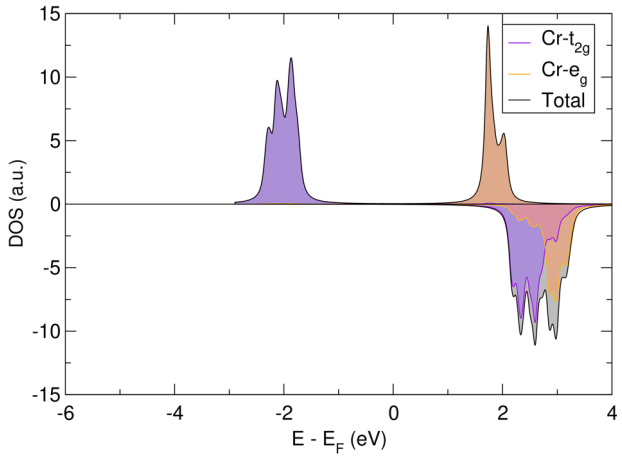

Fig. 2 *d*-only density of states. Purple and yellow denote Cr t_{2g} and e_g contributions, respectively. Coulomb matrix elements from Table 1 are used.

Table 2. Orbital-resolved exchange interactions from MFT in meV.

	$J_{t2g-t2g}$	J_{t2g-eg}	J	$J'_{t2g-t2g}$	J'_{t2g-eg}	J'
d only	−2.472	+0.508	−1.964	−0.137	+0.095	−0.042
$d+p$	−0.864	+2.620	+1.756	−0.046	+0.398	+0.352

CrI_3 we have applied the MFT to these HF solutions in a subsequent step (for details see Methods). The resulting orbitally resolved exchange couplings are given in Table 2 and show a strong antiferromagnetic (AFM) total coupling of $J=-1.964$ meV for nearest neighbors and $J'=-0.042$ meV for next-nearest neighbors, driven by a strong AFM $J_{t2g-t2g}$ interaction. This is obviously in contradiction to LSDA(+U) calculations and to all available experimental data. This wrong prediction can be understood from the Kugel–Khomskii (KK) formalism[15,38], which describes the total magnetic exchange as the sum of the t_{2g}–t_{2g} and t_{2g}–e_g contributions as $J(\mathbf{r})=J_{t2g-t2g}(\mathbf{r})+J_{eg-eg}(\mathbf{r})$ with

$$J_{t2g-t2g}(\mathbf{r}) \approx -\frac{2\tilde{t}^2_{t2g-t2g}(\mathbf{r})}{\tilde{U}} \tag{7}$$

$$J_{eg-eg}(\mathbf{r}) \approx \frac{2\tilde{t}^2_{t2g-eg}(\mathbf{r})\tilde{J}^{\mathrm{H}}}{(\tilde{U}+\Delta)(\tilde{U}+\Delta-\tilde{J}^{\mathrm{H}})}. \tag{8}$$

Here, $\tilde{t}_{t2g-t2g}(r)$ and $\tilde{t}_{t2g-eg}(r)$ are effective hopping matrix elements between the different orbital channels, Δ represents the crystal field splitting, and $\tilde{U}$ and $\tilde{J}^{\mathrm{H}}$ are the averaged Coulomb and Hund's exchange parameters. We immediately understand that $J_{t2g-t2g}$ is by definition of AFM nature and controlled only by the effective t_{2g}–t_{2g} hopping and the density–density channel of the Coulomb interaction ($\tilde{U}$). In contrast, the FM channel, J_{eg-eg}, is controlled by the effective t_{2g}–e_g hopping and both $\tilde{U}$ and J_H. By using the hopping values of our Wannier construction, given in the Supplementary Methods 5 and the averaged electron–electron interactions from the cRPA Coulomb tensor ($\tilde{U}\approx 3.4$ and $\tilde{J}_H\approx 0.4$ eV), we obtain an AFM intralayer exchange coupling in line with the MFT results. We carefully checked that this wrong KK prediction also holds in the case of the extended ($d+p$) basis by using effective hoppings from this models with and without p-mediated hopping, as summarized in the Supplementary Methods 5. In both cases, using only the direct hoppings as well as those after integrating our the I p contributions, we find that the effective nearest-neighbor $\tilde{t}_{t2g-t2g}$ is significantly larger than the $\tilde{t}_{t2g-eg}$ one so that the AFM coupling channels always dominate. Thus the correct microscopic origin of the FM coupling in CrI_3 cannot be described on a Cr d-only basis and can neither be modeled within the KK approach.

Table 3. Bare (v/j^{H}) and cRPA screened (U/J^{H}) local Coulomb interaction matrix elements from the ($d+p$) basis set in eV.

j/v	t_{2g}	t_{2g}	t_{2g}	e_g	e_g
t_{2g}	18.480	17.138	17.138	18.172	17.739
t_{2g}	*0.664*	18.479	17.138	18.172	17.738
t_{2g}	*0.664*	*0.664*	18.479	17.520	18.390
e_g	*0.485*	*0.485*	*0.804*	19.875	18.159
e_g	*0.697*	*0.697*	*0.378*	*0.858*	19.877
J^{H}/U	t_{2g}	t_{2g}	t_{2g}	e_g	e_g
t_{2g}	3.993	2.769	2.769	3.146	2.794
t_{2g}	*0.600*	3.993	2.769	3.146	2.794
t_{2g}	*0.600*	*0.600*	3.994	2.618	3.323
e_g	*0.460*	*0.460*	*0.714*	4.175	2.646
e_g	*0.629*	*0.629*	*0.375*	*0.765*	4.176

Density-density matrix elements are listed on the upper triangle and Hund's exchange elements are underlined and italic.

Extended ($d+p$)-basis

Motivated by the wrong predictions of the minimal Cr d-only model, we expanded the basis to also include the ligand p contributions. This ($d+p$)-basis has a significant impact to the local Cr Coulomb matrix elements as summarized in Table 3. Due to the presence of the I p orbitals the Cr d Wannier functions are more localized ($\Omega\approx 1$ Å^2) so that the resulting bare matrix elements are significantly enhanced as compared to the d-only case. Also the density–density matrix elements in the e_g channel are now larger than in the t_{2g} channel. The cRPA screening due to all other Cr and all I states, again significantly reduce all matrix elements in an orbital-dependent manner. The final intra-orbital density-density interactions are now on the order of 4 eV with inter-orbital elements of the order of 3 eV. Notably, the cRPA screened Hund's exchange interactions are also enhanced by the increased localization of the Cr d states. They are, however, still on the order of 0.5–0.7 eV and thus still significantly smaller than the common approximation of 0.9 eV. The nearest-neighbor cRPA screened density–density interactions are again nearly orbital independent $U_{01}\approx 1.4$ eV, while the maximal nearest-neighbor Hund's interactions is $J_{01}\approx 2$ meV.

As before in the d-only basis, the interaction term $\mathcal{H}^U$ of our Hamiltonian from Eq. (1) acts on the Cr d states only. The kinetic part, $\mathcal{H}^W$, however, now also includes I p contributions. Thus, to counter-act double counting effects we subtract here the double-counting potential defined in Eq. (14) from the Cr d states using a nominal $Cr^{3+}d$ occupation of $N^{\sigma}_{imp}=3$. This corrects for the relative positioning of the interacting Cr d bands with respect to the uncorrelated I p states.

The resulting HF DOS is shown in Fig. 3. In contrast to the d-only model we now find a DOS which is vastly reminiscent of the full ab initio GGAs + U results shown in Fig. 1 (see Supplementary Methods 3 for corresponding band structures). Next to the spin-splitting and -ordering also the full and sub-band gaps are in good agreement with GGAs + U predictions. Also, the atomic contributions to the unoccupied bands are very similar in our HF calculations as compared to the GGAs + U calculations. The most prominent difference is the orbital composition of the upmost

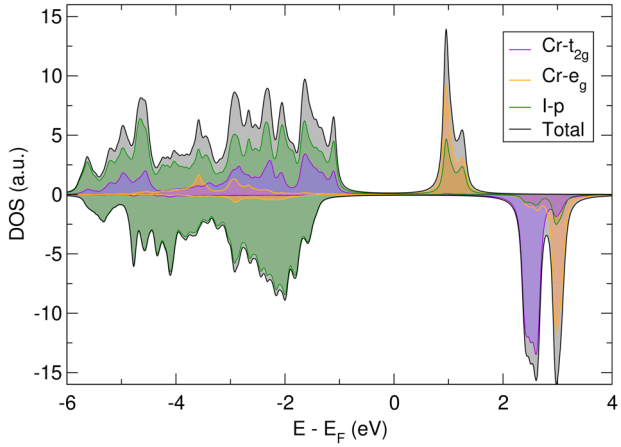

Fig. 3 Extended (*d*+*p*)-model density of states. Green, purple, and yellow denote I *p*, Cr t_{2g}, and e_g contributions, respectively. Coulomb matrix elements from Table 3 are used.

valence states. While the full ab initio GGAs + *U* calculations finds mostly I contributions here, our HF calculations also show a significant Cr admixture. At this stage, we cannot finally judge whether this difference results from our minimal localized basis sets, the fully rotationally invariant GGAs + *U* implementation we have used, or from the charge self-consistency within the full GGAs + *U* calculations, which we lack in our approach. Nevertheless, we see in the following that this model reliably predicts the magnetic properties of CrI_3 monolayer.

The orbital-resolved intralayer exchange couplings calculated using the MFT are given in Table 2. In contrast to the *d*-only model, the (*d* + *p*)-model gives the correct FM exchange coupling $J \approx 1.76$ meV ($J' \approx 0.35$ meV), similar to previously reported values from MFT calculations based on LSDA + *U* input[15]. To microscopically explore how the different Coulomb interaction channels (U, U', J^H) affect the electronic band structure and the magnetic properties, we present in Fig. 4 the bandwidths and positions together with the orbitally-resolved exchange interactions upon individual *reductions* of each Coulomb channel by 20%. Reducing the intra-orbital Coulomb interactions (ΔU) results in a lower spin splitting of the t_{2g} and e_g bands, similar to the single-orbital Hubbard model. The other two cases, namely, $\Delta U'$ and ΔJ^H, are more difficult to understand since these terms mix different types of orbitals. When reducing U', we observe a strong reduction of the splitting between the $t_{2g,\uparrow}/e_{g,\uparrow}$ manifolds, accompanied by a strong gap reduction of about 1 eV. In contrast, the splitting between the $t_{2g,\downarrow}/e_{g,\downarrow}$ manifolds is weakly affected by U' compared to the initial full cRPA case. Finally, when we reduce Hund's exchange J^H, the $t_{2g,\sigma}/t_{2g,\bar{\sigma}}$ and the $e_{g,\sigma}/e_{g,\bar{\sigma}}$ splittings are both reduced, while the splitting between the majority spin occupied $t_{2g,\uparrow}$ bands and empty $e_{g,\uparrow}$ bands increases with respect to the unperturbed case, leading to a small increase in the bandgap.

These band-structure renormalizations have non-trivial effects to the microscopic exchange interactions, which we depict in Fig. 4 (bottom panel) and which can be just partially understood within the KK formalism. In line with KK a reduction of U or U' yields an enhancement of the AFM $J_{t2g-t2g}$ channel, as shown in the ΔU and $\Delta U'$ columns of Fig. 4 (bottom panel), while modifications to J^H do not affect $J_{t2g-t2g}$ at all. Also in qualitative agreement with KK we find that a reduction of J^H reduces the FM J_{t2g-eg}. In contrast to the simple model predictions from KK we find from MFT that $J_{t2g-t2g}$ is slightly reduced upon reducing U while modifications to U' yields no modifications. This underlines the need for the full microscopic MFT in combination with an extended basis to quantitatively understand magnetism in CrI_3. We expect that just an extended model combining the

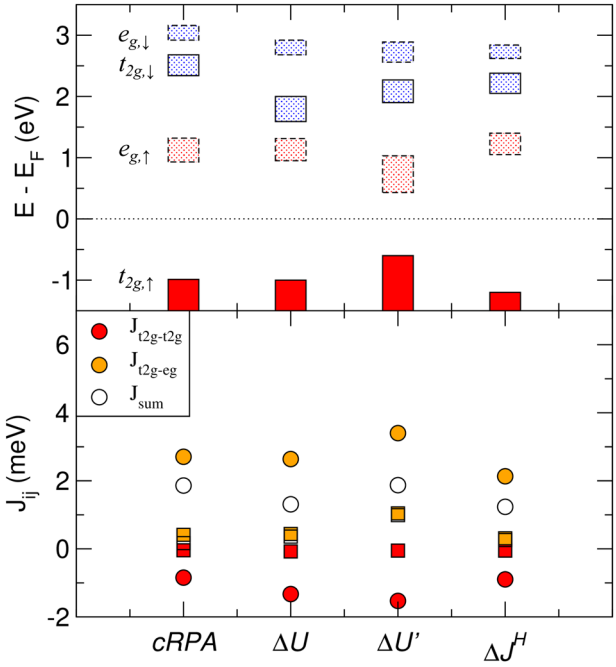

Fig. 4 Coulomb interaction effects to the electronic and magnetic properties of the (*d*+*p*)-model. a Electronic properties: red and blue stands for spin up and down polarized bands. Continuous and dashed lines correspond to t_{2g} and e_g bands, respectively. The dotted line indicates the Fermi energy position. The size of the boxes is related to the bandwidth. **b** Magnetic exchange interactions: circles and squares denote 1st and 2nd neighbor intra-layer exchange couplings obtained with the MFT. Red, orange, and empty circles stand for $J_{t2g-t2g}$, J_{t2g-eg}, and J_{sum} which is the sum of both interactions. For both, 1st and 2nd neighbors, t_{2g}–t_{2g} interactions are always AFM, while the t_{2g-eg} ones are FM.

super-exchange mechanism from the Goodenough-Kanamori description and the multi-orbital KK mechanism might yield a qualitatively understanding in line with our MFT findings, which will be studied separately. Here, we conclude that the extended (*d* + *p*)-basis together with the corresponding cRPA Coulomb matrix elements and using an HF solver results in a reliable band-structure and microscopically correct magnetic properties.

Substrate tunability

In the following, we proceed with the analysis of dielectric screening effects to the magnetic properties of CrI_3 monolayer. We investigate how a dielectric encapsulation, as depicted in the inset of Fig. 5a, modifies the Coulomb interactions in CrI_3 and how this affects its bands structure and eventually its microscopic magnetic properties.

Figure 5a summarizes how the orbital averaged local intra- and inter-orbital density-density as well as Hund's exchange matrix elements scale upon increasing the environmental screening (ϵ). Since ϵ affects the macroscopic monopole-like interactions only, U and U' are equally reduced by ϵ, while J^H is not modified at all. The resulting screening-induced effects will thus be a combination of the ΔU and $\Delta U'$ columns from Fig. 4.

In Fig. 5b, we show the HF DOS for three different values of ϵ. As discussed in the previous section, a decreasing U results in a reduction of the *d*-bands splitting $\Delta_{t_{2g,\sigma}/t_{2g,\bar{\sigma}}}$ and $\Delta_{e_{g,\sigma}/e_{g,\bar{\sigma}}}$ and a decrease of the inter-orbital Coulomb terms U' reduces the gap between $t_{2g,\uparrow}$ and $e_{g,\uparrow}$. The overall effect of increasing ϵ is thus to decrease all gaps between all sub-bands.

In Fig. 5c, we summarize the resulting effects to the magnetic properties. Upon increasing ϵ we find the total nearest-neighbor

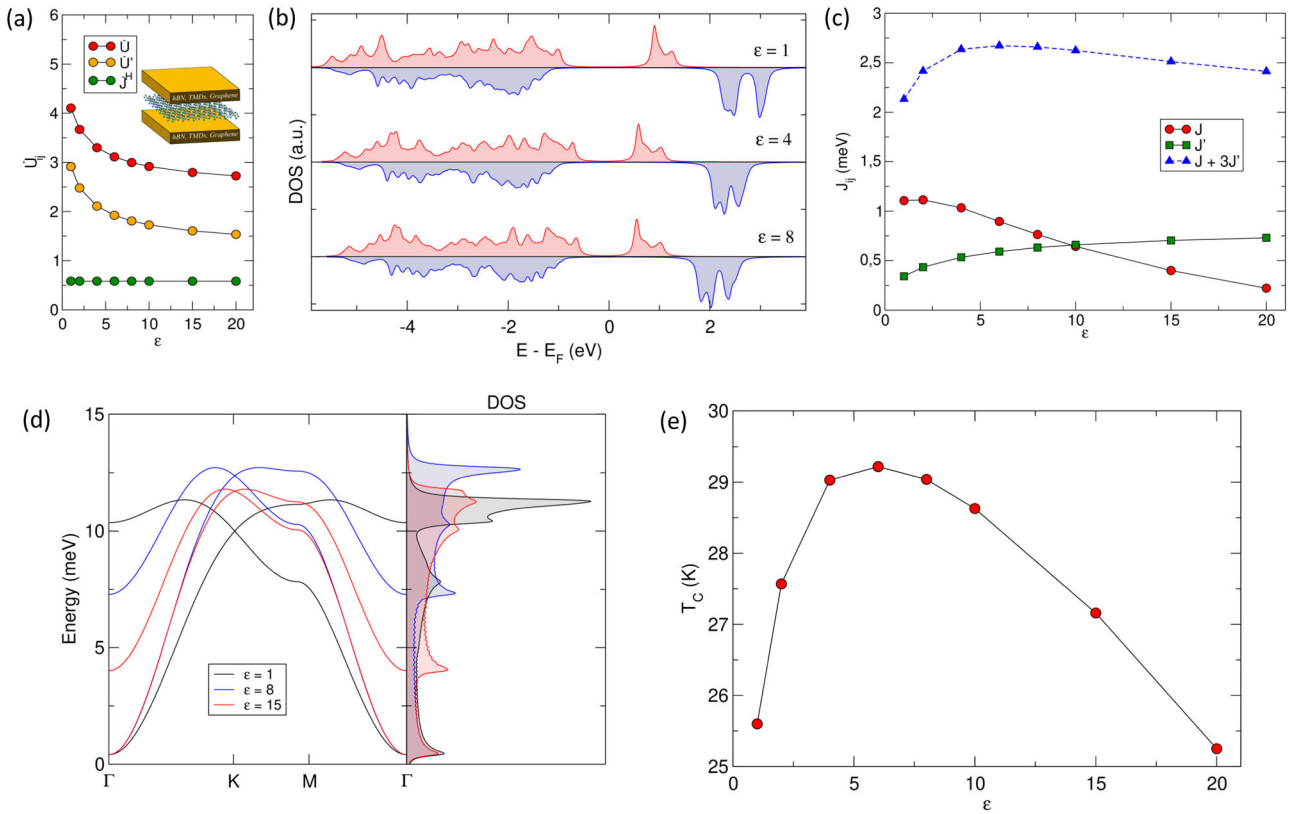

Fig. 5 Substrate screening effects. a Local Coulomb interactions: red, yellow, and green dots correspond to orbital-averaged intra- (U) and interorbital (U') Coulomb and Hund's exchange (J^H) interactions. The inset sketches an encapsulated monolayer CrI_3. **b** Electronic density of states for $\epsilon = 1$, $\epsilon = 4$, and $\epsilon = 8$. **d** Nearest and next-nearest neighbor magnetic exchange interactions J and J', respectively. The function $J + 3J'$ is shown for reference (see text for details). **e** Curie temperature.

Table 4. Orbital-resolved nearest- and next-nearest neighbor exchange interactions in CrI_3 monolayer calculated for different substrate dielectric screening constants in meV.

ε	$J_{t2g-t2g}$	J_{t2g-eg}	J	$J'_{t2g-t2g}$	J'_{t2g-eg}	J'
1	−0.864	2.620	1.756	−0.046	0.398	0.352
2	−1.116	2.956	1.840	−0.056	0.502	0.446
4	−1.452	3.198	1.746	−0.070	0.616	0.546
6	−1.694	3.280	1.586	−0.080	0.684	0.604
8	−1.882	3.308	1.426	−0.086	0.732	0.646
10	−2.032	3.314	1.282	−0.094	0.766	0.672
15	−2.308	3.298	0.990	−0.106	0.822	0.716
20	−2.496	3.270	0.774	−0.114	0.856	0.742

magnetic exchange decreasing from about $J \approx 1.1$ meV at $\epsilon = 1$ to $J \approx 0.2$ meV at $\epsilon = 20$, while the total next-nearest-neighbor exchange interaction slightly increases from $J' \approx 0.3$meV to $J' \approx 0.7$ meV. From Table 4, we understand that the decreasing trend in J is mostly driven by the enhancement of the AFM coupling within the $J_{t2g-t2g}$ channel, while the FM J_{t2g-eg} channel is barely affected. The next-nearest-neighbor J' is affected simultaneously by both, increasing FM and AFM microscopic exchange interactions. The FM channel grows, however, slightly faster so that the overall FM J' is enhanced. From this, we expect non-trivial effects of the environmental dielectric screening to the magnetic properties of CrI_3 monolayer relevant for most experimental setups dealing with supported and/or encapsulated films.

We start with the analysis of the magnon dispersion which reacts to the environmental screening differently in different parts of the Brillouin zone, as shown in Fig. 5d. At the Γ point the optical (high energy) branch is continuously lowered in energy upon increasing the screening, while the Dirac point at K is non-monotonously affected. Upon increasing ϵ from 1 to 8 the magnon energy at K first increases before it starts to decrease for larger ϵ. This behavior becomes clear from the spin-wave Hamiltonian Eq. (18) evaluated at K yielding the degenerated magnon-energies $E(K) = 3S(J + 3J' + \lambda)$. As one can see from Fig. 5c, $J + 3J'$ is indeed a non-monotonic function of ϵ with a maximum around $\epsilon = 6$. For the van-Hove singularities of both magnon branches at the M point we find similar non-trivial and non-monotonic behaviors with ϵ yielding a partially extended flat dispersion of the optical branch for intermediate ϵ. These non-trivial modifications to the magnon dispersion due to changes in ϵ are also reflected in the total magnon spectrum. Thereby we can relate each (partial) maximum in the magnon spectrum with either the Γ or the M point. As a result, these most prominent spectral features either monotonously decrease in energy or follow the non-monotonous trends from the M point.

In Fig. 5e, we additionally show the Curie temperature (T_c) for the same ϵ. Again, we find a non-monotonic behavior with an initially increasing T_c upon increasing the screening, a maximal T_c around $\epsilon = 6$, and a subsequently strongly decreasing trend. This trend approximately follows the spectral peak arising from the optical magnon branch at the M point. Due to its similarity with the K-point behavior, we conclude that the initial increasing trend in T_c is driven by the increasing trend of J' while the final decreasing trend is driven by J. The non-monotonic behavior of T_c is thus due to the non-monotonic interplay between nearest and next-nearest neighbor exchange interactions as a function of the environmental screening.

DISCUSSION

By combining state-of-the-art cRPA-based ab initio down-folding with our WFCE approach and the MFT method, we were able to study on a microscopic level how magnetism in CrI_3 monolayer builds up and how it is controlled by environmental screening properties. We showed that a mean-field description within the HF approximation to treat local Cr Coulomb interactions is sufficient to reproduce all characteristics of full ab initio GGAs + U calculations. From a thorough investigation of different minimal models, we understood that only an I p-based super-exchange mechanism together with the full multi-orbital t_{2g}–e_g structure of the Cr atoms allows for a realistic description of CrI_3 magnetism. A minimal model thus needs to involve all Cr d and I p states with sizable Coulomb interactions acting on the Cr d states. We also showed how environmental screening significantly reduces the local Coulomb interactions, which decisively modifies the electronic band structure and which finally yields non-monotonic changes to the microscopic magnetic exchange interactions. In detail, we found that dielectric encapsulation of the CrI_3 monolayer strongly reduces the nearest-neighbor exchange interaction, while the next-nearest-neighbor interaction is just slightly enhanced, which leaves remarkable footprints in the magnon spectral function and the Curie temperature.

These findings point to a variety of questions and problems to tackle in the future: On the modeling side, we found sizeable local Coulomb interactions as compared to the non-interacting bandwidth, possibly rendering dynamical mean-field theory or similar approaches necessary to capture all correlation effects[39–41]. Our extended ($d + p$)-model is an optimal starting ground for studies like these. Together with sizeable magnon–phonon couplings[42], light–matter interactions, and long-range Coulomb interaction effects[8,34], we can expect a plethora of correlation effects in this material to be found in the future.

In light of our findings on the environmental screening-induced modifications to the magnetic properties of monolayer CrI_3, we expect that magnetism in multilayer CrI_3 is more involving than expected. Next to electronic inter-layer hybridization effects, layer-dependent changes to Coulomb interactions seem to be important as well to gain a full understanding. Also, the role of anisotropic magnetic interactions, including both symmetric and asymmetric forms, needs to be studied in further detail. Substrate effects might be especially relevant in the context of Dzyaloshinskii–Moriya interactions (DMI), as they could be considerably enhanced by breaking/lowering inversion symmetries. At the same time, DMI appears to be promising for the stabilization of topological magnons[43] and skyrmionic phases[44,45] in chromium trihalides. Coulomb engineering of DMI could be considered using a computational scheme similar to the one proposed in ref. [46].

Finally, our findings render CrI_3 monolayer-based heterostructures with spatially structured environments a possibly fascinating playground to non-invasively structure the magnetic properties of layered magnetic materials similar to what has been discussed for correlation effects in layered semiconductors[20,21,23,47,48]. Together with the recent discovery of other 2D ferromagnets and antiferromagnets we thus expect that magnetic van der Waals heterostructures are the most promising platforms to engineer and design next-generation magnetic and opto-magnetic devices. The encapsulation-mediated tunability of the magnetic exchange has important implications in the future application of 2D ferromagnets as spintronic devices. The possibility to combine strong and weak FM regions on 2D ferromagnets using different substrates may find application as memory storage devices. Also, real-space manipulation of the magnon dispersion can open possibilities for low-consumption magnon-based devices.

METHODS

HF solver and double counting corrections

We approximately solve the Hamiltonian from Eq. (1) utilizing a variational single-particle wave function which allows for the breaking of the spin-symmetry. The variational energy is computed by decoupling the interaction terms in a conventional way. The resulting intra-atomic HF Hamiltonian takes the form of an effective single-particle one with local occupations n_i which need to be self-consistently evaluated. It can be divided into spin-conserving ($h^{\uparrow\uparrow}$, $h^{\downarrow\downarrow}$) and spin-mixing terms ($h^{\uparrow\downarrow}$, $h^{\downarrow\uparrow}$). In a general form, the full effective single-particle Hamiltonian reads

$$\mathcal{H} = \begin{bmatrix} h_{ii}^{\uparrow\uparrow} & h_{ij}^{\uparrow\uparrow} & h_{ii}^{\uparrow\downarrow} & h_{ij}^{\uparrow\downarrow} \\ h_{ji}^{\uparrow\uparrow} & h_{jj}^{\uparrow\uparrow} & h_{ji}^{\uparrow\downarrow} & h_{jj}^{\uparrow\downarrow} \\ h_{ii}^{\downarrow\uparrow} & h_{ij}^{\downarrow\uparrow} & h_{ii}^{\downarrow\downarrow} & h_{ij}^{\downarrow\downarrow} \\ h_{ji}^{\downarrow\uparrow} & h_{jj}^{\downarrow\uparrow} & h_{ji}^{\downarrow\downarrow} & h_{jj}^{\downarrow\downarrow} \end{bmatrix}, \tag{9}$$

where the i, j are orbital indices. The explicit expressions for each of the terms in the Hamiltonian are

$$h_{ii}^{\sigma\sigma} = U_{ii}\rho_{ii}^{\bar{\sigma}\bar{\sigma}} + \sum_{j\neq i}\left(U'_{ij}\rho_{jj}^{\bar{\sigma}\bar{\sigma}} + (U'_{ij} - J_{ij}^{\mathrm{H}})\rho_{jj}^{\sigma\sigma}\right), \tag{10}$$

$$h_{ij}^{\sigma\sigma} = -\sum_{j\neq i}\left((U'_{ij} - J_{ij}^{\mathrm{H}})\rho_{ji}^{\sigma\sigma} + J_{ij}^{\mathrm{H}}\rho_{ji}^{\bar{\sigma}\bar{\sigma}}\right), \tag{11}$$

$$h_{ii}^{\sigma\bar{\sigma}} = -U_{ii}\rho_{ii}^{\bar{\sigma}\sigma} - \sum_{j\neq i} J_{ij}^{\mathrm{H}}\rho_{jj}^{\bar{\sigma}\sigma}, \tag{12}$$

$$h_{ij}^{\sigma\bar{\sigma}} = -\sum_{j\neq i} U'_{ij}\rho_{ji}^{\bar{\sigma}\sigma}, \tag{13}$$

where ρ is the self-consistent density matrix containing the local occupations: $\rho_{ii}^{\sigma\sigma} = \hat{n}_i^{\sigma}$ and $\rho_{ij}^{\sigma\bar{\sigma}} = \langle d_{i,\sigma}^{\dagger} d_{j,\bar{\sigma}}\rangle$.

In order to minimize double-counting errors in the ($d + p$)-model due to interaction effects in the hopping matrix elements from the ab initio calculations, we subtract a double-counting potential based on the fully localized limit[25] approximation

$$\mu_{\mathrm{DC}}^{\mathrm{FLL}} = \bar{U}\left(N_{\mathrm{imp}} - \frac{1}{2}\right) - \bar{J}\left(N_{\mathrm{imp}}^{\sigma} - \frac{1}{2}\right) \tag{14}$$

where $\bar{U} = 1/(2l+1)\sum_i U_{ii}$ and $\bar{J} = 1/(4l^2 + 2l)\sum_{i\neq j} J_{ij}$ are the mean Coulomb and Hund exchange interactions obtained from the cRPA tensors, N_{imp} is the total occupancy of the Cr d-orbitals and $N_{\mathrm{imp}}^{\sigma}$ is the occupancy per spin ($N_{\mathrm{imp}}^{\sigma} = N_{\mathrm{imp}}/2$ in the paramagnetic ground state).

Magnetic force theorem

Magnetism in CrI_3 and related compounds results from a detailed interplay between local and non-local kinetic and local Coulomb interactions terms yielding an effective magnetic exchange between neighboring Cr atoms. Generally speaking, it can be understood as a super-exchange mechanism mediated by the ligand atoms which follows approximately the Goodenough–Kanamori mechanism[13]. With an approximate 90° angle between neighboring Cr–I–Cr atoms we thus expect an FM coupling. On a fully microscopic level, Kashin et al.[15] have recently shown, using the MFT, that the total FM exchange interaction results from an interplay between an AFM coupling channel between Cr t_{2g} orbitals and an FM channel between t_{2g} and e_g orbitals. In both, LSDA and LSDA + U calculations this interplay is dominated by the FM t_{2g}–e_g channel so that the total exchange interaction is also FM. To understand how this microscopic picture is affected by different choices of the target space, the different orbital channels of the Coulomb tensor, and by environmental screening effects, we follow Kashin et al.[15] and analyze the results of our HF calculation by means of the MFT[49], which allows us to calculate the orbitally resolved exchange interaction matrix elements via the second variations of the total energy with respect to infinitesimal rotations of the magnetic moments, leading to the expression[50,51]

$$J_{ij} = \frac{1}{2\pi S^2}\int_{-\infty}^{E_{\mathrm{F}}} d\varepsilon \sum_{\alpha\beta\gamma\delta} \Im\left[\Delta_i^{\alpha\beta} G_{ij}^{\beta\gamma\downarrow}(\varepsilon)\Delta_j^{\gamma\delta} G_{ji}^{\delta\alpha\uparrow}(\varepsilon)\right]. \tag{15}$$

Here, Latin (Greek) indices denote atomic (orbital) indices, respectively, E_{F} is the Fermi energy, and $\Delta_i^{\alpha\beta} = H_{ii}^{\alpha\beta\uparrow} - H_{ii}^{\alpha\beta\downarrow}$ is the exchange splitting matrix

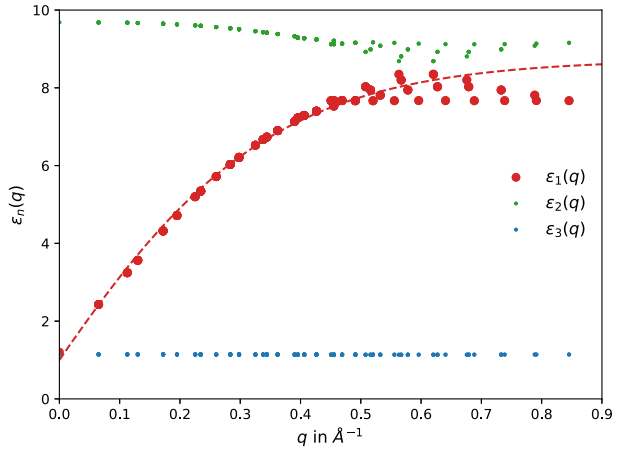

Fig. 6 Leading screening channels in the Wannier function continuum electrostatics approach. Red, green, and blue dots correspond to $\varepsilon_1(q)$, $\varepsilon_2(q)$, and $\varepsilon_3(q)$, respectively. $\varepsilon_1(q)$ is fitted using the expression from Eq. (25). The shown data is for the (d+p)-model.

defined in the orbital space. In Eq. (15), $G_{ij}^{\alpha\beta\sigma}(\varepsilon) = \sum_{\mathbf{k}} G_{\mathbf{k}}^{\alpha\beta\sigma}(\varepsilon) e^{i\mathbf{k}\cdot\mathbf{R}_{ij}}$ is the real-space Green's function, whose $\mathbf{k}$-space matrix representation reads

$$\mathcal{G}_{\mathbf{k}}^{\sigma}(\varepsilon) = \left[\varepsilon\mathcal{I} - \mathcal{H}_{\mathbf{k}}^{\sigma} + i\eta\mathcal{I}\right]^{-1}, \tag{16}$$

where $\mathcal{I}$ is the unity matrix, $\eta \to 0^+$ is a numerical smearing parameter, $\mathbf{R}_{ij}$ is the translation vector connecting atoms i and j, and $\mathcal{H}_{\mathbf{k}}^{\sigma}$ is the reciprocal-space Hamiltonian for spin $\sigma = \uparrow, \downarrow$, whose matrix elements are obtained in the basis of Wannier functions from our HF calculations. Positive and negative J_{ij} correspond here to FM and AFM couplings, respectively.

Magnetic properties

The spin Hamiltonian describing the exchange interactions between Cr atoms in CrI_3 can be written as:

$$\mathcal{H}_{spin} = \sum_i A(S_i^z)^2 + \frac{1}{2}\sum_{i,j} J_{ij}\mathbf{S}_i\mathbf{S}_j + \frac{1}{2}\sum_{i,j}\lambda_{ij}S_i^zS_j^z \tag{17}$$

where the first term A describes single-ion anisotropy, J_{ij} is the isotropic Heisenberg exchange, and λ_{ij} is the anisotropic symmetric exchange. To calculate the spin-wave spectrum, we transform Eq. (17) into a bosonic Hamiltonian using the linearized Holstein-Primakoff transformation with $A = 0$ and $\lambda = 0.09$ meV (see ref. [13])

$$\mathcal{H}_{SW} = \sum_i [3S(J+\lambda) + 6SJ']b_i^\dagger b_i - JS\sum_{\langle ij\rangle} b_i^\dagger b_j - J'S\sum_{\langle\langle ij\rangle\rangle} b_i^\dagger b_j \tag{18}$$

where J and J' correspond to nearest and next-nearest neighbor isotropic exchange couplings, and λ is the nearest neighbor anisotropic symmetric exchange. In $\mathbf{k}$-space, the Hamiltonian Eq. (18) for a honeycomb lattice takes the form

$$\mathcal{H}_{SW}(\mathbf{q}) = S\begin{pmatrix} \epsilon_0 - J'f_2(\mathbf{q}) & -Jf_1^*(\mathbf{q}) \\ -Jf_1(\mathbf{q}) & \epsilon_0 - J'f_2(\mathbf{q}) \end{pmatrix}, \tag{19}$$

where $\epsilon_0 = 3J + 6J' + 3\lambda$, and $f_1(\mathbf{q}) = \sum_{\mathbf{R}} e^{-i\mathbf{q}\cdot\mathbf{R}}$ and $f_2(\mathbf{q}) = \sum_{\mathbf{R}'} e^{-i\mathbf{q}\cdot\mathbf{R}'}$ are form factors with $\mathbf{R}$ and $\mathbf{R}'$ running over cells with nearest and next-nearest neighbor atoms, respectively. The diagonalization of this Hamiltonian yields the magnon spectrum, which reads

$$E(\mathbf{q}) = S(3J + 6J' + 3\lambda - J'f_2(\mathbf{q}) \pm J|f_1(\mathbf{q})|). \tag{20}$$

To calculate the magnetic T_c, we use Tyablikov's decoupling approximation (also known as RPA)[52] through the expression

$$T_C = \frac{1}{2}\frac{S(S+1)}{3Sk_B}\left(\frac{1}{N}\sum_{\mathbf{q}}\frac{1}{E(\mathbf{q})}\right)^{-1}. \tag{21}$$

Substrate screening

Next to the CrI_3 intrinsic properties, we aim to also understand the role of external screening properties such as resulting for substrate materials or capping dielectrics. To this end, we utilize our WFCE approach[19], which realistically modifies the CrI_3 Coulomb interaction tensor according to dielectric environmental screening and which has been shown before to reliably describe the environmental screening impact to layered materials[23,48]. In this way we will be able to understand how the electronic band structure and the microscopic magnetic properties are affected, e.g., by encapsulating CrI_3 with hBN or under the influence of bulk substrates.

We start with the non-local bare Coulomb interaction of the CrI_3 monolayer as obtained from our cRPA calculations in momentum space. Within a matrix representation $v_{\alpha\beta}(q)$ using a product basis $\alpha, \beta = \{n, m\}$ we can diagonalize the Coulomb tensor

$$v(q) = \sum_\nu v_\nu(q)|v_\nu(q)\rangle\langle v_\nu(q)| \tag{22}$$

with $v_\nu(q)$ and $|v_\nu(q)\rangle$ being the corresponding eigenvalues and eigenvectors of the Coulomb tensors and $q = |\mathbf{q}|$. Assuming that the eigenbasis does not drastically change upon the effects of the cRPA screening, we can thus represent the full cRPA Coulomb tensor as

$$U(q) = \sum_\nu \frac{v_\nu(q)}{\varepsilon_\nu(q)}|v_\nu(q)\rangle\langle v_\nu(q)|, \tag{23}$$

where $\varepsilon_\nu(q)$ is the corresponding pseduo-eigenvalues of the dielectric tensor describing the different screening channels. In Fig. 6 we show the first three $\varepsilon_\nu(q)$ as a function of momentum q and find that only one shows a significant dispersion, which we refer to as the "leading" eigenvalue in the following. This behavior becomes clear upon investigating the corresponding eigenvectors on the basis of the two Cr atoms in the long-wavelength limit, i.e., for $q \to 0$

$$|v_1(q)\rangle = \begin{vmatrix} +1 \\ +1 \end{vmatrix}\rangle, \qquad |v_2(q)\rangle = \begin{vmatrix} +1 \\ -1 \end{vmatrix}\rangle. \tag{24}$$

The leading eigenvalue $v_1(q)$ thus renders Coulomb penalties for monopole-like perturbations (all orbitally resolved electronic densities on both Cr atoms are in-phase), while the second eigenvalue $v_2(q)$ corresponds to Cr-Cr dipole-like Coulomb penalties. $\varepsilon_1(q)$ and $\varepsilon_2(q)$ thus correspondingly describe mono- and Cr-dipole-like screening. While the dipole-like screening from the environment is negligible, the mono-pole-like screening as rendered by $\varepsilon_1(q)$ is strongly affected. This classical electrostatic screening can be modeled by solving the Poisson equation for a dielectric slab of height h embedded in some different dielectric environment[19,53–55] yielding

$$\varepsilon_1(q) = \frac{\varepsilon_1^{(0)}\left[1 - \tilde{\varepsilon}_0^{(1)}\tilde{\varepsilon}_0^{(2)}e^{-2qh}\right]}{1 + \left[\tilde{\varepsilon}_0^{(1)} + \tilde{\varepsilon}_0^{(2)}\right]e^{-qh} + \tilde{\varepsilon}_0^{(1)}\tilde{\varepsilon}_0^{(2)}e^{-2qh}} \tag{25}$$

with

$$\tilde{\varepsilon}_0^{(1)} = \frac{\varepsilon_1^{(0)} - \varepsilon_{\text{sub}}^{\text{below}}}{\varepsilon_1^{(0)} + \varepsilon_{\text{sub}}^{\text{below}}}, \qquad \tilde{\varepsilon}_0^{(2)} = \frac{\varepsilon_1^{(0)} - \varepsilon_{\text{sub}}^{\text{above}}}{\varepsilon_1^{(0)} + \varepsilon_{\text{sub}}^{\text{above}}}. \tag{26}$$

For $\varepsilon_{\text{sub}}^{\text{above}} = \varepsilon_{\text{sub}}^{\text{below}} = 1$ this describes the leading dielectric function of a free-standing monolayer, which we can fit perfectly to the cRPA data, as shown in Fig. 6 and yielding $h \approx 5.2$ Å and $\varepsilon_1^{(0)} \approx 8.7$ (for the case of the (d+p)-model). With these fitting parameters, we can now modify the full cRPA Coulomb tensor to describe environmental screening rendered by finite $\varepsilon_{\text{sub}}^{\text{above}}$ and $\varepsilon_{\text{sub}}^{\text{below}}$. Due to the monopole-like character of this environmental screening, we only affect density-density Coulomb matrix elements in the very same way. Therefore Coulomb exchange elements, such as J^H are not affected by the substrate screening. In Supplementary Methods 4 we benchmark this approach to full cRPA calculations taking the screening from additional (strained) hBN layers into account.

DATA AVAILABILITY

The data that support the findings of this study is available from the corresponding author upon reasonable request.

CODE AVAILABILITY

All non-commercial numerical codes to reproduce the findings of this study are available from the corresponding author upon reasonable request.

Received: 8 March 2021; Accepted: 7 September 2021;
Published online: 05 October 2021

REFERENCES

1. Klein, D. R. et al. Probing magnetism in 2D van der Waals crystalline insulators via electron tunneling. *Science* **360**, 1218–1222 (2018).
2. Kezilebieke, S. et al. Topological superconductivity in a van der Waals heterostructure. *Nature* **588**, 424 (2020).
3. Cardoso, C., Soriano, D., García-Martínez, N. A. & Fernández-Rossier, J. Van der Waals spin valves. *Phys. Rev. Lett.* **121**, 067701 (2018).
4. Lyons, T. P. et al. Interplay between spin proximity effect and charge-dependent exciton dynamics in $MoSe_2$/$CrBr_3$ van der Waals heterostructures. *Nat. Commun.* **11**, 6021 (2020).
5. Ghazaryan, D. et al. Magnon-assisted tunnelling in van der Waals heterostructures based on $CrBr_3$. *Nat. Electron.* **1**, 344–349 (2018).
6. Cenker, J. et al. Direct observation of two-dimensional magnons in atomically thin CrI_3. *Nat. Phys.* **17**, 20 (2021).
7. Liu, T. et al. Spin caloritronics in a $CrBr_3$-based magnetic van der Waals heterostructure. *Phys. Rev. B* **101**, 205407 (2020).
8. Wu, M., Li, Z., Cao, T. & Louie, S. G. Physical origin of giant excitonic and magneto-optical responses in two-dimensional ferromagnetic insulators. *Nat. Commun.* **10**, 2371 (2019).
9. Soriano, D. & Katsnelson, M. I. Magnetic polaron and antiferromagnetic-ferromagnetic transition in doped bilayer CrI_3. *Phys. Rev. B* **101**, 041402 (2020).
10. Jiang, S., Shan, J. & Mak, K. F. Electric-field switching of two-dimensional van der Waals magnets. *Nat. Mater.* **17**, 406–410 (2018).
11. Jiang, S., Li, L., Wang, Z., Mak, K. F. & Shan, J. Controlling magnetism in 2D CrI_3 by electrostatic doping. *Nat. Nanotechnol.* **13**, 549–553 (2018).
12. Huang, B. et al. Electrical control of 2D magnetism in bilayer CrI_3. *Nat. Nanotechnol.* **13**, 544–548 (2018).
13. Lado, J. L. & Fernández-Rossier, J. On the origin of magnetic anisotropy in two dimensional CrI_3. *2D Mater.* **4**, 035002 (2017).
14. Zhang, W.-B., Qu, Q., Zhu, P. & Lam, C.-H. Robust intrinsic ferromagnetism and half semiconductivity in stable two-dimensional single-layer chromium trihalides. *J. Mater. Chem. C* **3**, 12457–12468 (2015).
15. Kashin, I. V., Mazurenko, V. V., Katsnelson, M. I. & Rudenko, A. N. Orbitally-resolved ferromagnetism of monolayer CrI_3. *2D Mater.* **7**, 025036 (2020).
16. Torelli, D. & Olsen, T. Calculating critical temperatures for ferromagnetic order in two-dimensional materials. *2D Mater.* **6**, 015028 (2019).
17. Besbes, O., Nikolaev, S., Meskini, N. & Solovyev, I. Microscopic origin of ferromagnetism in the trihalides $CrCl_3$ and CrI_3. *Phys. Rev. B* **99**, 104432 (2019).
18. Xu, C., Feng, J., Xiang, H. & Bellaiche, L. Interplay between Kitaev interaction and single ion anisotropy in ferromagnetic CrI_3 and $CrGeTe_3$ monolayers. *npj Comput. Mater.* **4**, 57 (2018).
19. Rösner, M., Şaşığlu, E., Friedrich, C., Blügel, S. & Wehling, T. O. Wannier function approach to realistic Coulomb interactions in layered materials and heterostructures. *Phys. Rev. B* **92**, 085102 (2015).
20. Rösner, M. et al. Two-dimensional heterojunctions from nonlocal manipulations of the interactions. *Nano Lett.* **16**, 2322–2327 (2016).
21. Raja, A. et al. Coulomb engineering of the bandgap and excitons in two-dimensional materials. *Nat. Commun.* **8**, 15251 (2017).
22. Steinhoff, A. et al. Exciton fission in monolayer transition metal dichalcogenide semiconductors. *Nat. Commun.* **8**, 1166 (2017).
23. Waldecker, L. et al. Rigid band shifts in two-dimensional semiconductors through external dielectric screening. *Phys. Rev. Lett.* **123**, 206403 (2019).
24. van Loon, E. G. C. P., Rösner, M., Katsnelson, M. I. & Wehling, T. O. Random phase approximation for gapped systems: role of vertex corrections and applicability of the constrained random phase approximation. *Phys. Rev. B* **104**, 045134 (2021).
25. Anisimov, V. I., Aryasetiawan, F. & Lichtenstein, A. I. First-principles calculations of the electronic structure and spectra of strongly correlated systems: the LDA + U method. *J. Phys.* **9**, 767 (1997).
26. Perdew, J. P., Burke, K. & Ernzerhof, M. Generalized gradient approximation made simple. *Phys. Rev. Lett.* **77**, 3865–3868 (1996).
27. Blöchl, P. E. Projector augmented-wave method. *Phys. Rev. B* **50**, 17953–17979 (1994).
28. Kresse, G. & Joubert, D. From ultrasoft pseudopotentials to the projector augmented-wave method. *Phys. Rev. B* **59**, 1758–1775 (1999).
29. Kresse, G. & Furthmüller, J. Efficiency of ab-initio total energy calculations for metals and semiconductors using a plane-wave basis set. *Comput. Mater. Sci.* **6**, 15 (1996).
30. Kresse, G. & Furthmüller, J. Efficient iterative schemes for ab initio total-energy calculations using a plane-wave basis set. *Phys. Rev. B* **54**, 11169–11186 (1996).
31. Mostofi, A. A. et al. wannier90: A tool for obtaining maximally-localised Wannier functions. *Comput. Phys. Commun.* **178**, 685 – 699 (2008).
32. Aryasetiawan, F. et al. Frequency-dependent local interactions and low-energy effective models from electronic structure calculations. *Phys. Rev. B* **70**, 195104 (2004).
33. Kaltak, M. Merging GW with DMFT, PhD Thesis, University of Vienna, 231 pp. http://othes.univie.ac.at/38099/ (2015).
34. Ke, L. & Katsnelson, M. I. Electron correlation effects on exchange interactions and spin excitations in 2d van der waals materials. *npj Comput. Mater.* **7**, 1–8 (2021).
35. Casula, M. et al. Low-energy models for correlated materials: Bandwidth renormalization from coulombic screening. *Phys. Rev. Lett.* **109**, 126408 (2012).
36. Slater, J. C. The theory of complex spectra. *Phys. Rev.* **34**, 1293–1322 (1929).
37. Şaşıoğlu, E., Friedrich, C. & Blügel, S. Effective Coulomb interaction in transition metals from constrained random-phase approximation. *Phys. Rev. B* **83**, 121101 (2011).
38. Kugel', K. I. & Khomskiĭ, D. I. The Jahn-Teller effect and magnetism: transition metal compounds. *Sov. Phys. Usp.* **25**, 231 (1982).
39. Kvashnin, Y. O., Rudenko, A. N., Thunström, P., Rösner, M. & Katsnelson, M. I. Dynamical correlations in single-layer CrI_3. Preprint at http://arxiv.org/abs/2012.13562 (2020).
40. Craco, L., Carara, S. S., Shao, Y.-C., Chuang, Y.-D. & Freelon, B. Mott localization in the van der Waals crystal CrI_3: a GGA+DMFT study. *Phys. Rev. B* **102**, 195130 (2020).
41. Yekta, Y. et al. Strength of effective Coulomb interaction in two-dimensional transition-metal halides MX_2 and MX_3 (M = Ti, V, Cr, Mn, Fe, Co, Ni; X = Cl, Br, I). *Phys. Rev. Mater.* **5**, 034001 (2021).
42. Tian, Y., Gray, M. J., Ji, H., Cava, R. J. & Burch, K. S. Magneto-elastic coupling in a potential ferromagnetic 2d atomic crystal. *2D Mater.* **3**, 025035 (2016).
43. Kvashnin, Y. O., Bergman, A., Lichtenstein, A. I. & Katsnelson, M. I. Relativistic exchange interactions in CrX_3 (X = Cl, Br, I) monolayers. *Phys. Rev. B* **102**, 115162 (2020).
44. Behera, A. K., Chowdhury, S. & Das, S. R. Magnetic skyrmions in atomic thin CrI_3 monolayer. *Appl. Phys. Lett.* **114**, 232402 (2019).
45. Ghosh, S., Stojić, N. & Binggeli, N. Comment on "Magnetic skyrmions in atomic thin CrI_3 monolayer" [Appl. Phys. Lett. 114, 232402 (2019)]. *Appl. Phys. Lett.* **116**, 086101 (2020).
46. Katsnelson, M. I., Kvashnin, Y. O., Mazurenko, V. V. & Lichtenstein, A. I. Correlated band theory of spin and orbital contributions to Dzyaloshinskii-Moriya interactions. *Phys. Rev. B* **82**, 100403 (2010).
47. Utama, M. I. B. et al. A dielectric-defined lateral heterojunction in a monolayer semiconductor. *Nat. Electron.* **2**, 60–65 (2019).
48. Steinke, C., Wehling, T. O. & Rösner, M. Coulomb-engineered heterojunctions and dynamical screening in transition metal dichalcogenide monolayers. *Phys. Rev. B* **102**, 115111 (2020).
49. Liechtenstein, A., Katsnelson, M., Antropov, V. & Gubanov, V. Local spin density functional approach to the theory of exchange interactions in ferromagnetic metals and alloys. *J. Magn. Magn. Mater.* **67**, 65 – 74 (1987).
50. Rudenko, A. N., Keil, F. J., Katsnelson, M. I. & Lichtenstein, A. I. Exchange interactions and frustrated magnetism in single-side hydrogenated and fluorinated graphene. *Phys. Rev. B* **88**, 081405 (2013).
51. Logemann, R., Rudenko, A. N., Katsnelson, M. I. & Kirilyuk, A. Exchange interactions in transition metal oxides: the role of oxygen spin polarization. *J. Phys.* **29**, 335801 (2017).
52. Rusz, J., Turek, I. & Diviš, M. Random-phase approximation for critical temperatures of collinear magnets with multiple sublattices: GdX compounds (X = Mg, Rh, Ni, Pd). *Phys. Rev. B* **71**, 174408 (2005).
53. Jena, D. & Konar, A. Enhancement of carrier mobility in semiconductor nanostructures by dielectric engineering. *Phys. Rev. Lett.* **98**, 136805 (2007).
54. Emelyanenko, A. & Boinovich, L. On the effect of discrete charges adsorbed at the interface on nonionic liquid film stability: charges in the film. *J. Phys.* **20**, 494227 (2008).
55. Keldysh, L. V. Coulomb interaction in thin semiconductor and semimetal films. *JETP Lett.* **29**, 658 (1979).
56. Momma, K. & Izumi, F. *VESTA3* for three-dimensional visualization of crystal, volumetric and morphology data. *J. Appl. Crystallogr.* **44**, 1272–1276 (2011).

ACKNOWLEDGEMENTS

We thank M. Kaltak for sharing his cRPA implementation with us. M.I.K. acknowledges support by European Research Council via Synergy Grant 854843—FASTCORR. D.S. thanks financial support from EU through the MSCA project Nr. 796795 SOT-2DvdW. ANR acknowledges partial support from the Russian Science Foundation, Grant No. 21-72-10136. Part of this work was carried out on the Dutch national e-infrastructure with the support of SURF Cooperative.

AUTHOR CONTRIBUTIONS

D.S. and M.R. conceived and designed the project. Calculations have been performed by D.S., A.N.R. and M.R. All authors contributed to the paper writing.

COMPETING INTERESTS

The authors declare no competing interests.

ADDITIONAL INFORMATION

Supplementary information The online version contains supplementary material available at https://doi.org/10.1038/s41524-021-00631-4.

Correspondence and requests for materials should be addressed to M. Rösner.

Reprints and permission information is available at http://www.nature.com/reprints

Publisher's note Springer Nature remains neutral with regard to jurisdictional claims in published maps and institutional affiliations.